Optomechanical Coupling and Damping of a Carbon Nanotube Quantum Dot

N. Hüttner[,1] S. Blien[,1] P. Steger[,1,†] A.N. Loh,[1] R. Graaf,[1] and A.K. Hüttel[1,2,*]

[1]*Institute for Experimental and Applied Physics, University of Regensburg, Universitätsstr. 31, 93053
Regensburg, Germany*
[2]*Department of Applied Physics, Aalto University, Puumiehenkuja 2, 02150 Espoo, Finland*

Carbon nanotubes are excellent nanoelectromechanical systems, combining high resonance frequency, low mass, and large zero-point motion. At cryogenic temperatures they display high mechanical quality factors. Equally they are outstanding single-electron devices with well-known quantum levels and have been proposed for the implementation of charge or spin qubits. However, the integration of these devices into microwave optomechanical circuits is hindered by a mismatch of scales between typical microwave wavelengths, nanotube segment lengths, and nanotube deflections. As experimentally demonstrated recently by Blien *et al.* [Nat. Comm. **11**, 1363 (2020)], coupling enhancement via the quantum capacitance allows this restriction to be circumvented. Here we extend the discussion of this experiment. We present the subsystems of the device and their interactions in detail. An alternative approach to the optomechanical coupling is presented, allowing the mechanical zero-point motion scale to be estimated. Further, the mechanical damping is discussed, hinting at hitherto unknown interaction mechanisms.

I. INTRODUCTION

Optomechanics [1] and its manifold branches allow the characterization and manipulation of both macroscopic and nanoscale mechanical systems. Readily available techniques now include ground-state cooling [2,3] and squeezing [4] of nanomechanical states, displacement sensing at and beyond the standard quantum limit [5], and on-chip optical data processing [6]. Optomechanical techniques and formalisms have been applied to a wide range of material systems, from single atoms in traps to macroscopic interferometer mirrors [1].

Suspended single-wall carbon nanotubes (CNTs) have been shown to reach high quality factors of up to 5×10^6 [7,8] as mechanical resonators in a cryogenic environment. At the same time, they are excellent quantum dots and clean electronic quantum mechanical model systems, and transport spectroscopy at millikelvin temperatures has led to a large number of topical publications [9–11]. The observation of strong coupling between single-electron tunneling and the motion of the macromolecule [12,13] has initiated a further field of research [14–16], as has the integration of CNTs into circuit cavity quantum electrodynamics experiments [17,18].

Regarding the combination of the two fields, experimental approaches for optomechanics with CNTs at optical/visible frequencies exist [19–22]. However, since the photon energy exceeds the typical energy range of trapped electronic quantum states at low temperature, excitonic states, or even the electronic bandgap, they are fundamentally incompatible with Coulomb blockade experiments. Consequently, this frequency range needs to be excluded from consideration in all experiments where the electronic confinement within the nanotube plays a role.

The small dimensions of typical single-electron devices prevent effective integration into microwave optomechanical systems via conventional mechanisms relying only on radiation pressure [1,23]. This mismatch of scales, critical for quasi-one-dimensional objects as compared to, for example, nanomechanical drum resonators [3,24], becomes immediately obvious when comparing the typical microwave wavelength and thereby resonator size, approximately 1 cm for $f_c \sim 5$ GHz, the typical length of a suspended CNT quantum dot of approximately 1 µm, and the typical deflection of such a suspended nanotube of approximately 1 nm.

Recently, we have shown that the large variation in quantum capacitance of a CNT in the Coulomb blockade regime enhances the optomechanical coupling by several orders of magnitude at a suitable choice of working point [25]. Using optomechanically induced (in)transparency [26,27], a single photon coupling of up to $g_0 = 2\pi \times$ 95 Hz was measured. Here, we expand upon the data

———
*andreas.huettel@ur.de
†Current address: Department of Physics, Lancaster University, Lancaster LA1 4YB, United Kingdom.

evaluation and discussion of [25] and characterize a wide range of interactions in the device already partly presented there—between the mechanical resonator, the microwave resonator, and the quantum dot in the Coulomb blockade regime. Combining different types of measurements, we provide an extended model, which allows us to estimate, for example, the zero-point motion amplitude of the CNT, further discuss consistency of the resulting device parameters, and characterize the mechanical damping mechanisms.

II. DEVICE AND MEASUREMENT SETUP

Our device, shown in Fig. 1(a), combines a superconducting coplanar microwave cavity with a suspended CNT quantum dot, in this way acting as optomechanical hybrid structure. Coupling between the two subsystems is mediated via a gate electrode. This gate electrode, buried below the nanotube, is connected to the center conductor of the microwave resonator close to its input coupling capacitance (i.e., at one of the electric field and voltage antinodes).

The CNT and the coplanar waveguide (CPW) resonator form separate circuits, coupling to each other only capacitively. The CNT displays Coulomb blockade oscillations of conductance as a function of gate voltage, but also acts as a high-Q mechanical oscillator. Initially, the CNT is characterized via standard low-frequency quantum dot transport spectroscopy [9,28], and the resonator via a gigahertz transmission measurement.

A. Niobium coplanar resonator

The microwave-optical subsystem of our device is given by a coplanar half-wavelength resonator [29–31]. On a high-resistivity (greater than 10 kΩ cm) float-zone silicon substrate with a 500-nm thermally grown surface oxide, a uniform niobium layer is sputter-deposited. Using standard optical lithography followed by reactive ion etching, an impedance-matched CPW with in/out couple bond pads at both ends for transmission measurement is defined; see Fig. 1(a). Its center conductor **3** is interrupted by gaps twice; see **2** and **5** in Fig. 1(a), forming a $\lambda/2$-type resonant cavity for transmission measurement. The gap width determines the coupling capacitances C_{in} and C_{out} across which the resonator is driven and read out; the distance between the gaps defines the resonator length $\ell = 10.5$ mm and with it on first order the fundamental resonance frequency.

Close to the coupling capacitances (i.e., at the voltage antinodes), a stublike extension of the center conductor connects to the gate electrode for the CNT, see **B** in Fig. 1(b) and the discussion below. Additionally, at its midpoint (i.e., the voltage node of the fundamental electromagnetic resonance mode), the center conductor is connected to a dc feed, **4** in Fig. 1(a), for the application of a gate bias [32]. This dc feed, similar to the connections
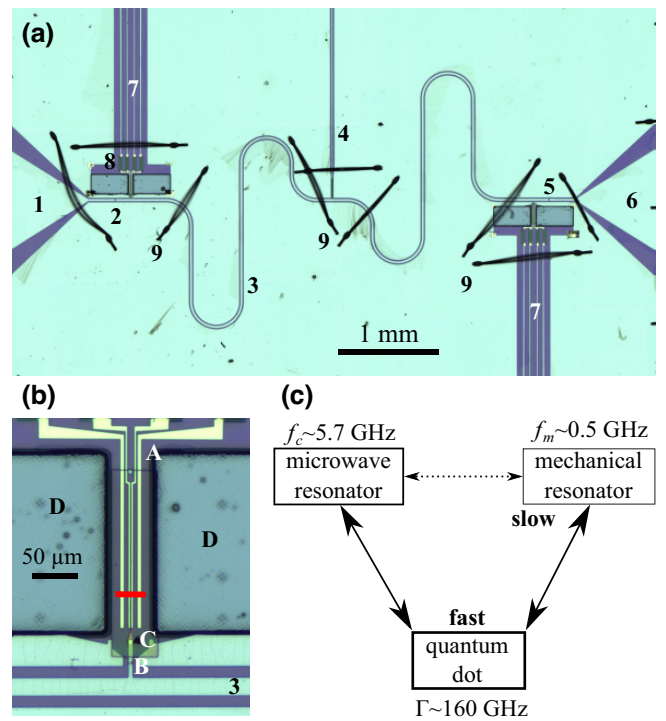

FIG. 1. (a) Optical microscope overview image of the device, combining a coplanar waveguide resonator and two carbon nanotube deposition areas (only one of which was used in the measurement). 1, gigahertz input port; 2, input coupling capacitor; 3, coplanar waveguide resonator; 4, dc (gate voltage) connection; 5, output coupling capacitor; 6, gigahertz output port; 7, dc (source, drain, and cutting electrode) connections; 8, meander inductance filters; 9, bond wires for potential equilibration. (b) Detailed image of the nanotube deposition area. A, Source, drain, and (2×) outer cutting electrodes; B, gate finger connected to the coplanar resonator; C, gate isolation [transparent, cross-linked poly(methyl methacrylate)]; D, deep-etched (approximately 10 μm) region to allow for fork deposition of the nanotubes. The red line corresponds to the cut sketched in Fig. 3(a) and thus also to one possible location of a carbon nanotube. (c) Scheme detailing the interactions between nanotube and microwave field and the relevant frequencies. Microscope images adapted from [25], Fig. S1.

to the CNT discussed below, contains a thin, resistive gold meander with an approximate length of 3 mm acting as radio-frequency block.

Figure 2(a) schematically shows the cryogenic measurement setup, Fig. 2(b) an example transmission measurement $|S_{21}|^2$ of the resonator at base temperature $T \simeq 10$ mK of the dilution refrigerator, and Fig. 2(c) the corresponding transmission phase. The measured value includes cable damping of approximately −8 dB, the attenuators of −53 dB distributed over the stages of the dilution refrigerator for input cable thermalization, a low-temperature high electron mobility transistor amplifier at the 1.8 K stage with amplification of 30 dB, and a room temperature
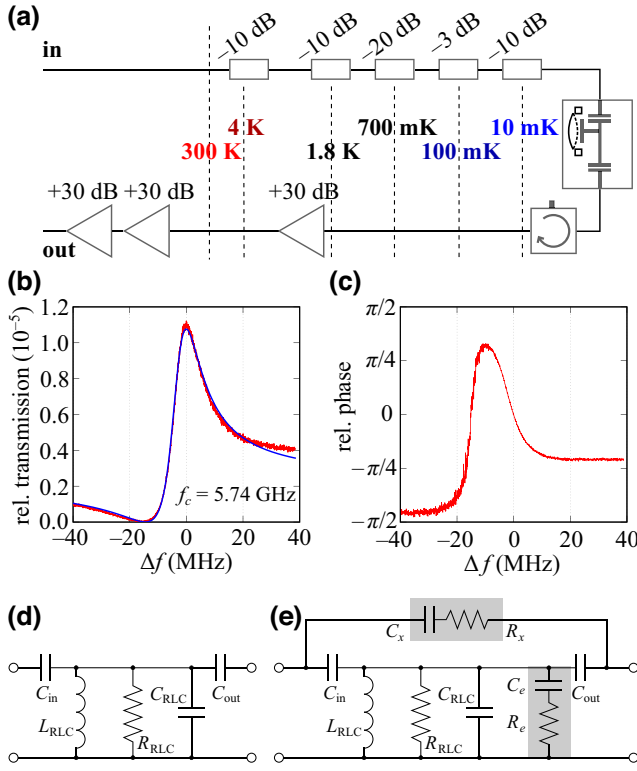
FIG. 2. (a) Schematic gigahertz transmission measurement wiring of the dilution refrigerator, with attenuators for thermalization at each temperature stage on the input side, a cryogenic circulator (QuinStar QCY-060400CM00), a cryogenic amplifier (CalTech CITCRYO1-12A), and two room-temperature amplifiers at the output side. (b),(c) Transmission amplitude (b, data identical to [25], Fig. S9) and phase angle (c) of the measured coplanar resonator near resonance. The maximum transmission is −49.6 dB. The blue line is a fit using the phenomenological Fano model of Eq. (1). (d) Generic replacement *RLC* circuit of a coupled waveguide resonator measured in transmission [33]. (e) Extended replacement *RLC* circuit taking into account the carbon nanotube circuitry (via C_e and R_e) and cross-talk through the sample space (via C_x and R_x).

amplifier chain with a total amplification of approximately 60 dB.

Any CPW resonator can be translated into a lumped element *RLC* replacement circuit with identical resonant frequency $\omega_c = 1/\sqrt{L_{RLC}C_{RLC}}$ [33]. Figure 2(d) displays the simplest such variant for a $\lambda/2$ resonator measured in transmission [33]. The relationship $C_{RLC} = C_c/2$ (for the fundamental resonance only) effectively expresses that fields are not distributed equally along the CPW cavity, with an electric field node of this mode at its center.

Our measurement displays a clear Fano shape instead of the Lorentzian naively expected from the circuit of Fig. 2(d), indicating the presence of additional nonresonant transmission channels parallel to the coplanar resonator. In terms of a circuit model, such a Fano shape can be taken into account by introducing a parallel channel [34]; see

Fig. 2(e) and, in particular, C_x and R_x there. In addition, the figure introduces the impact of a coupled CNT and its electrodes, via C_e and R_e.

Comparisons have, however, shown that it makes no significant difference for our evaluation whether we calculate the S_{21} parameter for Fig. 2(e) analytically or work with a conceptually much simpler Fano model that absorbs C_e and R_e into C_{RLC} and R_{RLC} and takes C_x and R_x into account via a complex constant offset of S_{21}. In this model one obtains for the transmission [35,36]

$$ S_{21} = A \left(\frac{1}{1 + 2iQ_c(f - f_0)/f_0} + re^{i\theta} \right), \qquad (1) $$

where r and θ describe transmission amplitude and phase of the parallel, parasitic channel. Using a fit of Eq. (1), we obtain from the measurement a resonance frequency of $f_c = 5.74$ GHz and a resonance width of $\Gamma_c = 2\pi \times 11.6$ MHz, corresponding to a quality factor of $Q_c = 497$. Table I collects these device parameters by way of an overview.

In comparison with similar experiments from literature [23,37], the observed quality factor of our device is surprisingly low. Given that we have already fabricated CPW resonators with intrinsic quality factors of $Q_i \simeq 2 \times 10^5$ [38], the limitation is likely not given by resonator or substrate material or the resonator patterning process *per se*. Two factors contribute here. On the one hand, the multiple lithographic steps required for device fabrication lead to an increased chance of defects and contamination. Examples can be seen in Fig. 1(a) near the center of the CPW resonator, with veillike structures from fluorinated resist residues. Testing of multiple resonator devices has shown that such structures on top of the center conductor lead to a significant decrease of the quality factor.

TABLE I. Overview of the microwave cavity parameters.

Microwave cavity			
Cavity resonance frequency	[a]	f_c	5.74005 GHz
Cavity line width	[a]	Γ_c	$2\pi \times 11.6$ MHz
Cavity quality factor	$2\pi f_c/\Gamma_c$	Q_c	497
Cavity total capacitance	[b]	C_c	1750 fF
Replacement capacitance	$C_c/2$	C_{RLC}	875 fF
Replacement inductance	$1/(4\pi^2 f_c^2 C_{RLC})$	L_{RLC}	879 pH

[a]Obtained from a fit using Eq. (1).
[b]Calculated CPW capacitance from lithographic geometry of the waveguide and substrate material properties, and neglecting the much smaller C_{in}, C_{out}, and C_g.

On the other hand, the dc electrodes of the CNT deposition areas couple out part of the gigahertz signal from the coplanar resonator. While the gold meanders in the dc connections are intended as inductive high-frequency blocks, they are also resistive, leading to signal dissipation. Future device design will replace them with reflective low-pass filters [39] to avoid signal loss near the cavity resonance.

B. Carbon nanotube quantum dot

The device includes two regions where a CNT can be deposited onto contacts next to the CPW resonator; see Fig. 1(b). For the measurements presented here, only one of these was used. The detailed CNT growth and transfer procedure, adapted from works of other research groups in the field, has already been discussed in detail elsewhere [25,40,41]. After deposition, the nanotube freely crosses a trench of width $L = 1$ μm between two gold electrodes acting as source and drain. A finger gate at the bottom of the trench, below an isolating poly(methyl methacrylate) layer, is connected to the CPW resonator for coupling, and can also be used to apply a dc gate voltage; see Fig. 3(a).

When varying the applied gate voltage, we observe the typical Coulomb blockade oscillations of a quantum dot [9,28,42]; see Fig. 3(b). In this overview plot of the dc current, $|I(V_g, V_{sd})|$, an apparent electronic bandgap around $V_g = -0.6$ V is flanked on both sides by Coulomb blockade oscillations. A detail measurement of the differential conductance in the parameter region later used for the optomechanical measurements, Fig. 3(c), displays multiple differential conductance lines in single-electron tunneling, possibly related to longitudinal vibration [43–47], electronic excitations, or trap states in the contacts. No clear fourfold shell pattern of the Coulomb oscillations can be observed, possibly due to small-scale defects or disorder of the CNT.

In the parameter region discussed in detail below we obtain via evaluation of the Coulomb blockade data of Figs. 3(b) and 3(c) [28] capacitances of $C_g = 2.6$ aF and $C_\Sigma = 9.8$ aF for the quantum dot, and with these the gate conversion factor $\alpha = 0.27$; see also Table II. In addition, we can estimate the total tunnel rate of quantum dot–lead coupling from the zero-bias conductance peak broadening. A value of $\Gamma = 160$ GHz, corresponding to 0.69 meV, is consistent both with conductance and (as discussed later) optomechanical coupling [25]. This makes electronic tunneling the fastest relevant time scale in our coupled system
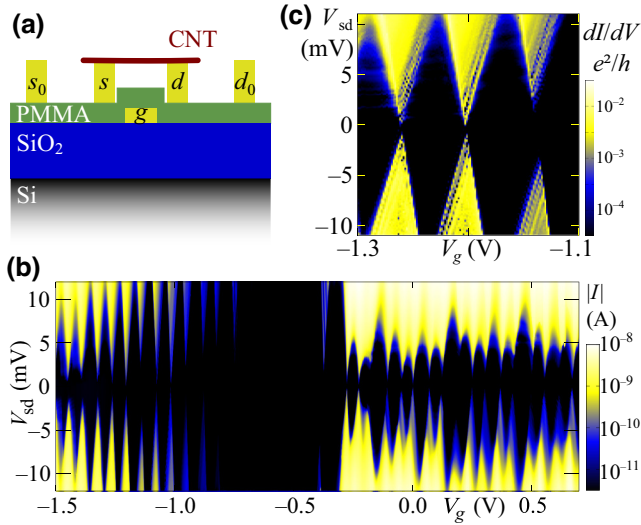

FIG. 3. (a) Schematic side view of the carbon nanotube lying across contacts and gate and forming a typical quantum dot device. A possible location for this trace cut is given in Fig. 1(b) with a red line. (b) Overview plot of the current $|I_{sd}(V_g, V_{sd})|$ as a function of gate voltage V_g and bias voltage V_{sd}, showing Coulomb blockade oscillations on both sides of the presumed electronic bandgap of the nanotube [larger range of the data of [25], Fig. 2(c)]. (c) Detail from (b); plot of the numerically obtained differential conductance $dI_{sd}/dV_{sd}(V_g, V_{sd})$ in the parameter region later characterized in gigahertz measurements, again displaying the typical regions of Coulomb blockade and of single-electron tunneling.

TABLE II. Overview of the carbon nanotube parameters.

Nanotube quantum dot			
Gate capacitance	a	C_g	2.6 aF
Total capacitance	a	C_Σ	9.8 aF
Gate lever arm	C_g/C_Σ	α	0.27
Total tunnel rate	a	Γ	160 GHz
Effective electronic length		ℓ_{eff}	140 nm
Nanotube mech. resonator			
Mode 1 curvature	b	a_1	-20.42 kHz/V^2
Mode 1 center voltage	b	$V_{g0,1}$	-2.64234 V
Mode 1 center frequency	b	$f_{0,1}$	502.592 MHz
Mode 2 curvature	b	a_2	6.41 kHz/V^2
Mode 2 center voltage	b	$V_{g0,2}$	7.47759 V
Mode 2 center frequency	b	$f_{0,2}$	500.537 MHz
Normal mode splitting	b	Δf_{min}	450 kHz
Suspended length of nanotube	c	ℓ	1 μm
Radius of nanotube	d	r	2 nm
Effective mass	d	m	4.8×10^{-21} kg
Imprinted tension	e	T_0	4.8 nN
Mech. line width		Γ_m	$\lesssim 2\pi \times 50$ kHz
Quality factor	$2\pi f_m/\Gamma_m$	Q_m	$\gtrsim 10^4$

[a]From Coulomb blockade characterization near $V_g = -1.2$ V; see Fig. 3(b).
[b]From the coupled classical harmonic oscillator fit using Eq. (3); see also Fig. 4(a).
[c]Lithographic distance of the contact electrodes.
[d]Estimated, typical values.
[e]Calculated via Eq. (4).

[cf. Fig. 1(c)], clearly exceeding the cavity and mechanical resonance frequencies.

An estimation of the gate capacitance via a simple wire-over-plane model [25,48], using an averaged relative dielectric constant $\epsilon_r = 2$ and a gate distance of $d = 450$ nm, coincides with the gate capacitance from Coulomb blockade for a reduced length $\ell_{\mathrm{eff}} = 140$ nm of the nanotube; we call this the *effective electronic length* of our CNT quantum dot. This models, for example, the reduction caused by depletion regions in pn barriers, or more generally corrects for geometry deviations.

C. Driven vibrational motion of the nanotube

The behavior of a CNT quantum dot as high-Q nanomechanical resonator at cryogenic temperatures has been discussed in many recent works [7,8,12,15,16,50,51]. The dominant external force acting on the nanotube as a suspended beam is given by the electrostatic force of the gate charge acting on the quantum dot charge; the restoring force stems from the tension, either built-in or deflection induced, and the bending rigidity of the macromolecule. Overall deflection leads to an elongation, an increase in the tension, and thus an increase in its mechanical resonance frequency [52,53].

The fundamental bending mode resonance frequency of a suspended nanotube scales with the segment length L as $1/L^2$; from the literature we typically expect it in the range of 50 MHz $\leq f_m \leq$ 100 MHz for an $L = 1$ µm long nanotube [7,49,52–54]. The device presented here shows two resonances around 500 MHz; see Fig. 4(a). In the plot, a lock-in amplifier is used to amplitude-modulate the applied rf driving signal at $f_{\mathrm{am}} = 72$ Hz and pick up the corresponding modulation of the low-frequency current through the nanotube; while slightly less sensitive than the so-called frequency modulation technique [55], this method retains a more natural resonance shape.

A thorough search at lower drive frequencies led to no additional results. In combination with the weak gate voltage dependence, this indicates a high built-in tension imprinted onto the CNT during fabrication. Its origin likely lies in the transfer of CNTs into the resonator circuit [25,40,41]. The nanotubes are grown on a quartz fork and lowered onto the contact electrodes until a finite current is measured. Then they are locally cut by resistive heating with a large current through it. The heating only affects the nanotube and its immediate surroundings, with the macromolecule slightly melting the gold contacts and attaching there; traces of this have been observed in microscope images of test structures. The force pulling the nanotube over the contacts leads to an eventual imprinted tension in the device. This effect is also illustrated by the SEM image of Fig. 5. It shows a different, subsequently produced device, where, however, similar fabrication steps and lithographic geometries have been used. Between source and
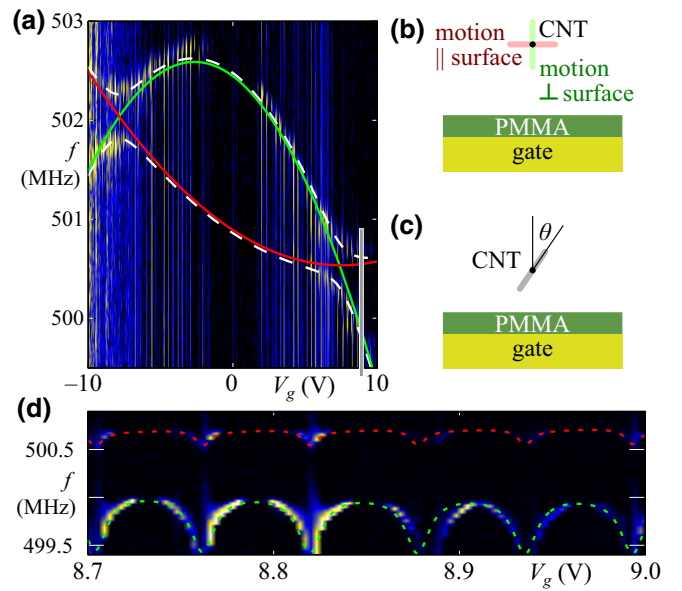

FIG. 4. (a) Large-scale plot of the mechanical resonance detection result, combined with a fit of two coupled vibration modes of parabolic gate voltage dependence. An amplitude-modulated ($f_{\mathrm{am}} = 72$ Hz) driving signal at frequency f is applied via a contact-free antenna [7,12,14,49]; the plot shows the resulting modulation of the rectified current via the lock-in signal dI/dP_{rf}. The dashed lines are a fit using Eq. (3); see Table II for the fit parameters. The red and green solid lines show the two corresponding vibration modes in the absence of coupling. Data already shown in [25], Figs. S6 and S7. (b) Schematic drawing (view along the carbon nanotube axis) of the two transversal vibration modes parallel and perpendicular to the device surface. (c) Schematic of a transversal vibration mode with arbitrary orientation angle θ. (d) Coulomb oscillations of mechanical resonance frequency [12,13], in the parameter region marked in (a) with a gray rectangle, and using the same measurement scheme as in (a). The dashed lines indicate a fit with subsequent Coulomb oscillations as described in the text. Raw data already shown in [25], Fig. S8.

drain electrode, the visible nanotube (CNT) is stretched straight, while it is clearly nontensioned outside these electrodes.
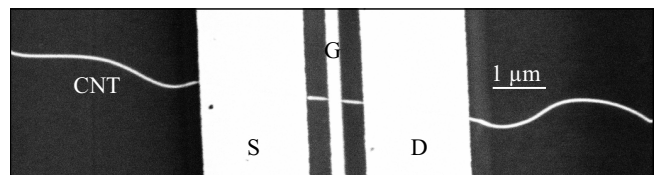

FIG. 5. Detailed SEM image of a different device fabricated later, but having a similar fabrication procedure and geometry. A carbon nanotube lies across source (S), gate (G), and drain (D) electrode. Between the source and drain electrodes it is stretched straight; outside them it bends.

Cooling of the device from room temperature to base temperature of the dilution refrigerator leads to a thermal contraction of the silicon substrate. Even though a negative axial coefficient of expansion for CNTs has been theoretically predicted for a long time [56–58], surprisingly few experiments exist [59]. What data there are confirm a negative thermal expansion, hinting that the cooling of the nanotube and the expansion coefficient mismatch with the substrate should not introduce tension (but rather counteract tension or induce buckling).

Our observed modes in the tensioned case correspond in first approximation to the fundamental transversal vibration parallel to the device surface and toward the gate [60] [see Fig. 4(b)]; only for the latter does electrodynamic softening of the vibration mode [60–62] contribute to the large-scale gate voltage dependence of the resonance frequency, inverting the dispersion at low gate voltage. The negative curvature term is absent for motion parallel to the chip surface, where only the tension-induced frequency increase is observed. Note that this model, treating the nanotube as a two-dimensional oscillator, still simplifies away many physically relevant details, from the deflection envelope along the nanotube all the way to screwlike motions or buckling [51].

As fit functions in Fig. 4(a), two coupled classical harmonic oscillator modes with general parabolic dispersion

$$f_i(V_g) = a_i(V_g - V_{g0,i})^2 + f_{0,i} \quad (2)$$

are chosen ($i = 1, 2$; solid lines in the figure), leading to fit functions

$$f_{\pm}(V_g) = \sqrt{\frac{1}{2}\left(f_1^2 + f_2^2\right) \pm \frac{1}{2}\sqrt{\left(f_1^2 - f_2^2\right)^2 + 4W^2}} \quad (3)$$

(dashed lines in the figure). Here, W parametrizes the coupling between the two modes. In the evaluated voltage range, this model describes the large-scale gate voltage dependence of the resonance frequencies very well; the resulting fit parameters can be found in Table II. The coupling of the vibration modes via the tension of the nanotube induces a sizeable mode splitting of 0.45 MHz, similar in magnitude to previous observations [63].

With the effective mass $m = 4.8 \times 10^{-21}$ kg, $f_{\max} \simeq 501.5$ MHz, and the suspended length $\ell = 1\,\mu$m, we obtain using the relation

$$f_{\max} = \frac{1}{2}\sqrt{\frac{T_0}{m\ell}} \quad (4)$$

the remarkably large fabrication-imprinted tension (i.e., the axial tension of the nanotube in the absence of electrostatic forces) $T_0 = 4.8$ nN.

Assuming now that the contributions to the spring constant add up linearly, we can use the difference in curvature of the two modes to isolate the electrostatic softening effects alone. With $a_s = a_1 - a_2$, using [62,64]

$$-a_s = f_{\max}\frac{C_g''\ell}{4\pi^2 T_0}, \quad (5)$$

we obtain $C_g'' = \mathrm{d}^2 C_g/\mathrm{d}x^2 = 1.0 \times 10^{-5}$ F/m². The wire-over-plane model, with the length of the wire rescaled as discussed above to the effective electronic length $\ell_{\mathrm{eff}} = 140$ nm, leads to $C_g'' = 2.7 \times 10^{-6}$ F/m², smaller by a factor of approximately 4.

While one may typically expect symmetric behavior around $V_g = 0$ V [65], static charges, for example, at the substrate surface can explain a common offset of the extrema of both modes. However, this provides no straightforward explanation for the relative shift of the two modes in V_g, with the frequency maximum of the electrostatically softened mode at $V_g = -2.64$ V and the minimum of the nonsoftened mode at $V_g = 7.48$ V.

As initially shown in [12,13], in CNTs Coulomb blockade effects also have a strong impact on mechanical resonances. A corresponding detailed measurement of the two mechanical modes is shown in Fig. 4(d) and will be discussed below.

III. INTERACTION OF THE SUBSYSTEMS

A. Microwave resonance shift due to Coulomb blockade

As already mentioned above, the effective replacement circuit capacitance C_{RLC} [see Fig. 2(d)] is directly related to the geometric capacitance C_c of the CPW resonator, taking into account the spatial distribution of electric fields. For our $\lambda/2$ resonator, we calculate a geometric capacitance of $C_c = 1750$ fF, neglecting the small and constant coupling capacitances. In the case of the fundamental mode of our $\lambda/2$ resonator and its field distribution, this translates to $C_{\mathrm{RLC}} = C_c/2 = 875$ fF [30]. With the resonance frequency, we obtain a corresponding replacement circuit inductance of $L_{\mathrm{RLC}} = 879$ pH, which in the following is assumed constant.

The gate-voltage-dependent contribution of the quantum dot to the total replacement circuit capacitance $\Delta C_{\mathrm{RLC}}(V_g)$ can be written as quantum capacitance

$$\Delta C_{\mathrm{RLC}}(V_g) = C_q = \frac{\partial Q_g}{\partial V_g} = \alpha\frac{\partial Q_{\mathrm{dot}}}{\partial V_g} \quad (6)$$

with α the gate conversion factor of the quantum dot as introduced above. It describes the response of the gate charge Q_g to a gate voltage fluctuation [18,66,67]. In Coulomb blockade, C_q is effectively zero since the charge on the quantum dot is constant for small voltage variations. In contrast, a maximum of C_q is reached at the position of a conductance peak where the charge on the quantum dot
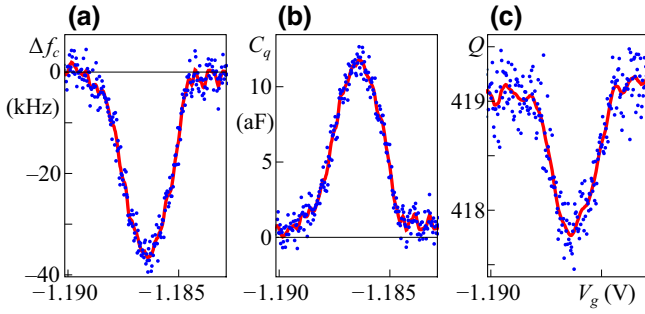
FIG. 6. Impact of a Coulomb oscillation of conductance of the carbon nanotube quantum dot on the coplanar waveguide resonator: (a) resonance frequency shift $\Delta f_c(V_g)$, (b) quantum capacitance $C_q(V_g)$ calculated from $\Delta f_c(V_g)$, and (c) quality factor $Q_c(V_g)$ of the coplanar waveguide resonator as a function of the applied static gate voltage V_g. The red curves show in each case a moving average. All data points are obtained by fitting Eq. (1) to frequency-dependent transmission measurements $|S_{21}(f)|^2$.

varies. This becomes directly visible as a reduction of the cavity resonance frequency f_c.

A corresponding measurement is shown in Fig. 6(a). For each value of the gate voltage V_g across a Coulomb oscillation, a trace of the CPW resonator transmission $S_{21}(f)$ has been recorded. Fitting the transmission data with Eq. (1), we obtain the resonance frequency $f_c(V_g)$ and its change $\Delta f_c(V_g) = f_c(V_g) - f_c^0$ induced by the quantum capacitance [Fig. 6(a)], and the resonator quality factor $Q_c(V_g)$ [Fig. 6(c)]. Assuming constant L_{RLC}, we then translate $\Delta f_c \approx 36$ kHz into a change in replacement circuit capacitance $\Delta C_{\mathrm{RLC}}(V_g) = C_q \approx 10$ aF [see Fig. 6(b)]. Remarkably, this effective value is larger than the bare geometric gate capacitance of the CNT to the gate finger $C_g = 2.6$ aF.

The quality factor $Q_c(V_g)$ of the microwave resonator is clearly reduced when the nanotube quantum dot is in single-electron conduction; see Fig. 6(c). This effect is not covered by the circuit model, but can be explained as follows. As discussed below in Sec. III C in detail, we can estimate the voltage amplitude of the driven cavity and with it the energy stored in the cavity. Using the data of Fig. 9(b), we obtain $V_{\mathrm{ac}} = 9.5$ mV and $E_{\mathrm{cav}} = 246$ eV for the parameters of Fig. 6. This ac voltage amplitude is consistent with the width of the Coulomb oscillation in Fig. 9(a), Sec. III C, at a nominal generator drive power of 10 dBm.

The dip in the cavity Q-factor Q_c indicates an additional energy loss per microwave period induced by single-electron tunneling. The loss can be estimated as

$$\Delta E = E_{\mathrm{cav}} \left(\frac{1}{Q_c^{\mathrm{CB}}} - \frac{1}{Q_c^{\mathrm{SET}}} \right) = 1.76 \text{ meV}. \qquad (7)$$

Applying a model initially developed for nanoelectromechanical systems [68], we assume that, due to the finite
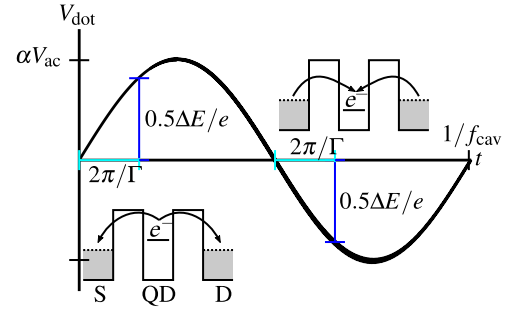

FIG. 7. Dissipation mechanism for the drop in Q_c observed in Fig. 6(c); see text. Due to a finite tunnel rate Γ and a corresponding delay effect, electrons are pumped from a lower to a higher potential by the microwave signal.

tunnel rate Γ connecting the quantum dot to its leads, the quantum dot occupation only follows the potential oscillation with a delay. In this way, electrons are pumped from lower to higher energy states, resulting in an energy loss for the microwave resonator.

Figure 7 illustrates the mechanism as well as the expected average energy ΔE lost during one microwave period: an electron tunnels from the quantum dot to the electrodes on average after a time $2\pi/\Gamma$, extracting $0.5\Delta E$ from the microwave resonator. The same amount of energy is then extracted again since on average only $2\pi/\Gamma$ after the gate potential falls below the source/drain Fermi energy an electron enters the dot. Coulomb blockade ensures that during one microwave cycle at most one electron undergoes this process. The combined tunnel rate of the contacts Γ is thus related to ΔE as

$$\frac{1}{\Gamma} = \frac{1}{\omega_c} \arcsin \left(\frac{\Delta E}{2\alpha V_{\mathrm{ac}} e} \right). \qquad (8)$$

For $\alpha V_{\mathrm{ac}} = 2.52$ mV and the parameters given in the measurement of Fig. 6(c), we obtain a tunnel rate of $\Gamma = 101$ GHz, in reasonable agreement with the previous estimate from Coulomb blockade of $\Gamma = 160$ GHz for this parameter.

B. Transmission phase based quantum capacitance detection

At or close to the microwave cavity resonance f_c, the transmission phase of the microwave resonator is highly sensitive to the drive frequency deviation $\Delta f = f - f_c$; see Fig. 2(b). A slight shift of the resonance frequency, for example, due to changes of the resonator environment, becomes equally visible as a transmission phase shift, with an approximate linear relation. This allows the resonator to be efficiently probed and with it the quantum capacitance of the adjunct nanotube system, a technique that has already been applied successfully to CNTs; see [18,66]. Neither the resonance shift (maximum 40 kHz) nor the
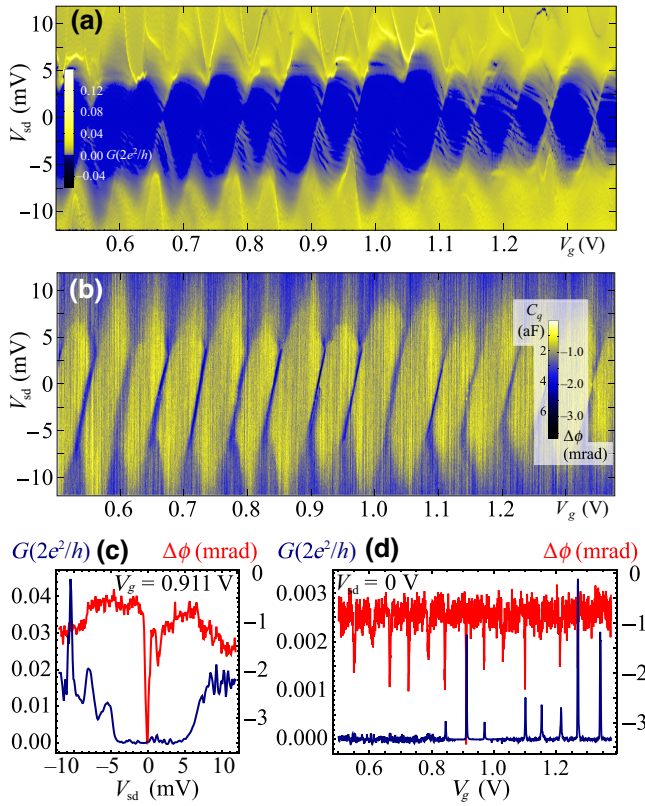
FIG. 8. (a) Direct current conductance and (b) simultaneously measured gigahertz transmission phase at $f = 5.73957$ GHz, as a function of the applied gate voltage V_g and bias voltage V_{sd} across the carbon nanotube quantum dot. The transmission was measured with a vector network analyzer input filter bandwidth of 2 Hz. (c), (d) Trace cuts from (a),(b), for constant gate voltage $V_g = 0.911$ V (c) and constant bias voltage $V_{sd} = 0$ V (d), respectively. Dark blue/left axis, differential conductance; red/right axis, gigahertz transmission phase.

change in resonance width from Q (maximum 65.5 kHz) identified in Fig. 6 can move our working point significantly relative to the greater than 10 MHz wide cavity resonance or significantly change the slope of the linear relation. With $f_c = 5.739\,57$ GHz and $Q_c = 495$ we obtain a phase shift of $\phi/\Delta f = 0.144$ mrad/kHz.

A corresponding measurement is shown in Fig. 8. Figures 8(a) and 8(b) plot the simultaneously measured dc conductance and microwave transmission phase, as a function of applied gate voltage V_g and bias voltage V_{sd}, over a range of several Coulomb oscillations. Figures 8(c) and 8(d) are trace cuts from the measurement, for (c) constant gate voltage $V_g = 0.911$ V and constant bias voltage $V_{sd} = 0$.

The Coulomb oscillations and with them the oscillatory behavior of the quantum capacitance in V_g are immediately visible. In Fig. 8 we use an input filter bandwidth of the vector network analyzer (VNA) of $\Delta f_{IF} = 2$ Hz, corresponding to an integration time per point of the order of

0.5 s. From the phase noise $\Delta\varphi \sim 0.2$ mrad of the trace cut of Fig. 8(c) we can estimate a measurement sensitivity of 2 aF or better; see also [18]. While this does not reach the resolution of Fig. 6(b), it is recorded significantly faster.

In Fig. 8(b), the phase shift highlights a preferred edge of the single-electron tunneling regions as the parameter region where the time-averaged charge of the quantum dot changes by one electron. This indicates that the tunneling rates from the quantum dot to source and drain differ significantly; in single-electron tunneling the time-averaged charge is close to one of the neighboring Coulomb blockade regions. Charging of the quantum dot predominantly happens when the quantum dot potential crosses the Fermi edge of the contact with the higher tunneling rate. Similar observations have already been made on quantum dots with asymmetrically coupled reservoirs [18,69]; for an in-depth analysis of charging and tunnel rates see [69], where a quantum point contact charge detector is used to obtain an equivalent signal.

C. Impact of gigahertz signals on the quantum dot

The impact of a microwave signal in the resonator on dc (or, more precisely, time-averaged/rectified) transport through the quantum dot (i.e., the reverse effect compared to above discussion) is shown in Fig. 9. Since the electronic tunnel rates and thus the Coulomb oscillation width $\Gamma_{est} \simeq 163$ GHz [25] clearly exceed the drive frequency $f_d \simeq 5$ GHz, we can treat the microwave signal as a classical oscillating gate voltage. In a first approximation, this signal, too fast for our low-frequency circuit to follow, thus effectively widens the observed Coulomb oscillations.

This is demonstrated in Fig. 9(a) for a resonant and in Fig. 9(b) for an off-resonant cavity drive. In Fig. 9(a), increasing P_{out} additionally leads to a peak current increase, indicating that at the resulting large photon numbers in the cavity the approximation of broadening of the peak only breaks down. For the off-resonant case in Fig. 9(b), the peak current decreases with applied power, and we can model the impact of the ac signal numerically by averaging a (near) zero-drive gate trace over a sinusoidal gate voltage of given amplitude.

In detail, we extract a trace $I_0(V_g)$ at small or zero drive amplitude (here, at $P_{out} = -10$ dBm) and then numerically find the ac gate voltage amplitude V_g^{ac} such that the average

$$I_{driven}(V_g) = \frac{1}{2\pi}\int_0^{2\pi} I_0\left(V_g + V_g^{ac}\sin(\varphi)\right)\,d\varphi \qquad (9)$$

best fits to a measured trace $I(V_g)$ at finite drive amplitude. Example results are shown in Fig. 9(c), for data measured at $P_{out} = 22$ dBm, 19 dBm, 16 dBm and the resulting best ac voltages for the broadening $V_g^{ac} = 0.53$ mV, 0.37 mV, 0.25 mV. The lowest set of points shows the reference trace at $P_{out} = -10$ dBm. Figure 9(d)
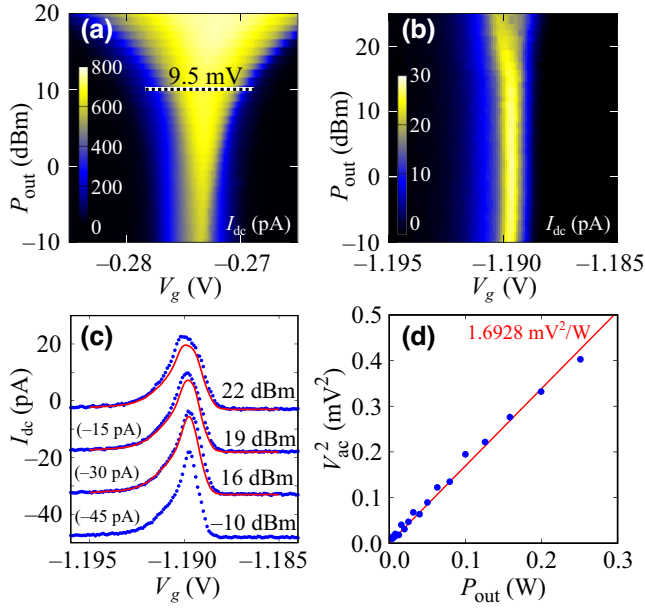
FIG. 9. (a),(b) Broadening of a Coulomb oscillation while (a) a resonant and (b) an off-resonant microwave drive at differing output power is applied to the microwave resonator: dc current I_{dc} as a function of gate voltage V_g and rf generator output power P_{out}. (a) $V_{sd} = 2$ mV, $f_d = 5.739\,57$ GHz; (b) $V_{sd} = 0.15$ mV, $f_d = 5.239\,89$ GHz; data already shown in [25], Fig. S10(a). (c) Data points: trace cuts $I_{dc}(V_g)$ from (b) at $P_{out} = 22$ dBm, 19 dBm, 16 dBm, -10 dBm. Solid lines: fits of the numerically broadened low-power trace at -10 dBm, resulting in a modulation ac voltage V_{ac} (see the text for the model). The different drive powers are offset for clarity. (d) Plot of the square of the modulation voltage V_{ac}^2 extracted from the data of (b), as a function of the applied generator output power P_{out}, and linear fit, resulting in a proportionality factor of 1.6928 mV^2/W; data already shown in [25], Fig. S10(b).

plots the square of the ac voltage as a function of generator power P_{out}, demonstrating that these values are proportional as expected.

We approximate that due to the proximity of the nanotube transfer regions to the coupling capacitors of the CPW resonator the ac gate voltage amplitude is equal to the voltage amplitude at the resonator antinode (i.e., at the coupling capacitor). This allows an estimate of the photon number in the resonator as a function of applied drive power. Using the linear fit of Fig. 9(d) (red sideband drive) and the replacement circuit capacitance $C_{RLC} = 875$ fF as discussed above, a generator drive power of $P_{out} = 0.1$ W $= 20$ dBm translates to a voltage amplitude of $V_g^{ac} \simeq 0.41$ mV and to $n_c \simeq 21\,300$ resonator photons. A more detailed discussion of error sources for the estimation can be found in Appendix A.

Note that the measurements of Figs. 9(b)–9(d) have been performed with an off-resonant drive of the cavity. In the case of a resonant drive, the increased photon occupation (larger by a factor of $|S_{21}(f_0)/S_{21}(f)|^2$) leads to

a correspondingly stronger ac signal and thus broadening; see Fig. 9(a). Calculating the expected peak width for $P_{out} = 10$ dBm at resonance gives 9.5 mV, which is in good agreement with the observation in Fig. 9(a); see the scale bar in the figure. Additionally, the maximum current increases at large power, which is in clear disagreement with our simple broadening model. For tunneling through a single, discrete level in the quantum dot, heating of the electron gas in the contacts leads to a decrease in the current [70]. This leaves as explanation for the increase either accessing excited states as additional transport channels via the broadened Fermi distribution of the contacts or more complex processes such as (multi)photon-assisted tunneling.

D. Interaction of vibration and Coulomb blockade

Figure 4(d) shows a detailed measurement of the driven mechanical resonances, corresponding to a zoom of the region marked in Fig. 4(a) with a gray bar. Here, the impact of the Coulomb oscillations on the two mechanical modes becomes clearly visible [12]. Comparison with Fig. 4(a) allows us to conclude that the lower mode with 499.4 MHz $\leq f \leq 500$ MHz is predominantly the globally softening (perpendicular to the device surface) mode and the upper mode with 500.5 MHz $\leq f \leq 500.3$ MHz is predominantly the globally hardening (parallel to the device surface) mode. The measurement is still near the mode anticrossing at $V_g \simeq 7.5$ V, however, such that a finite mode mixing cannot be excluded.

The dashed lines in Fig. 4(c) correspond to fits to the extracted resonance positions. We simplify the Coulomb oscillations as a sequence of six equidistant Lorentzians in conductance, with the corresponding increase in the time-averaged number of electrons in the quantum dot $\langle N \rangle (V_g)$ from the resonant tunneling picture. Since the oscillation at $V_g \simeq 8.88$ V does not fit into this equidistant peak scheme (which is not particularly surprising for a CNT quantum dot with significant quantum mechanical contributions to the addition energy), we ignore the data points around this one Coulomb oscillation. The overall fit function used for each of the two mechanical modes ($i = 1, 2$) is

$$f_i(V_g) = a_{1,i} + a_{2,i}V_g + a_{3,i}\langle N \rangle (V_g) + a_{4,i}\frac{d\langle N \rangle}{dV_g} \quad (10)$$

where, in particular, $a_{4,i}$ captures the *local* electrostatic softening through the Coulomb blockade oscillation, expressed in [12] for the spring constant as

$$a_{4,i} \propto \Delta k \propto \left(\frac{dC_g}{dx}\right)^2 \quad (11)$$

[Eq. (S5) there, with other control parameters such as V_g constant].

For a vibration mode whose motion does not change the gate capacitance, no local capacitive softening is expected, and indeed the higher-frequency mode in Fig. 4(c) shows a much smaller coupling to the Coulomb oscillations. From the fits, we obtain a ratio $a_{4,2}/a_{4,1} = 0.29$, leading to a ratio of the capacitance sensitivities

$$\frac{\mathrm{d}C_g/\mathrm{d}x_2}{\mathrm{d}C_g/\mathrm{d}x_1} = \sqrt{0.29} \simeq 0.54,$$

which would be fulfilled for two relatively perpendicular vibration modes both rotated by $\arctan(0.54) \simeq 30°$ to the device surface normal. For future measurements it would be interesting to trace a mode anticrossing as in Fig. 4(a) in more detail and extract the evolution of the couplings and their ratio as a function of gate voltage in this nanoelectromechanical model system.

IV. QUANTUM CAPACITANCE ENHANCED OPTOMECHANICS

A. Introduction

Dispersive coupling is both experimentally and theoretically the most widely researched mechanism for obtaining an optomechanical system [1]. Here, mechanical displacement causes a change in resonance frequency of an electromagnetic/optical resonator. In a microwave optomechanical system, this typically happens via a modification of the capacitance of a *LC* circuit; one of the capacitor electrodes is the mechanically active element.

While optomechanical effects in a combined nanotube–microwave resonator system as shown in Fig. 10(a) can in principle occur due to geometrical capacitance changes alone, a quick estimate already shows that the resulting coupling parameters are tiny [25]. Essentially, this is a manifestation of a mismatch of scales. Working frequencies for CPW resonators are typically in the range 4–8 GHz. With this one obtains wavelengths and resonator sizes of the order of ~1 cm. A CNT segment with ballistic conduction, where electrons can be confined to single, well-separated and unperturbed quantum levels, typically has a length of no more than about 1 μm. Mechanical deflections of such a segment as vibrational resonator are around 1 nm (at strong driving) [49] and 1 pm (zero-point motion) [25]. Obviously, a deflection less than 1 nm will barely affect the geometric properties of a resonator 1 cm in size.

In the following, the nonlinear charging characteristic of the quantum dot embedded in the nanotube is used for amplification of the coupling. As demonstrated above, it leads to a gate-voltage-dependent, locally strong quantum capacitance contribution, which can dominate geometric effects. The mechanical oscillation is slow compared to both tunnel rates and microwave resonance frequency,
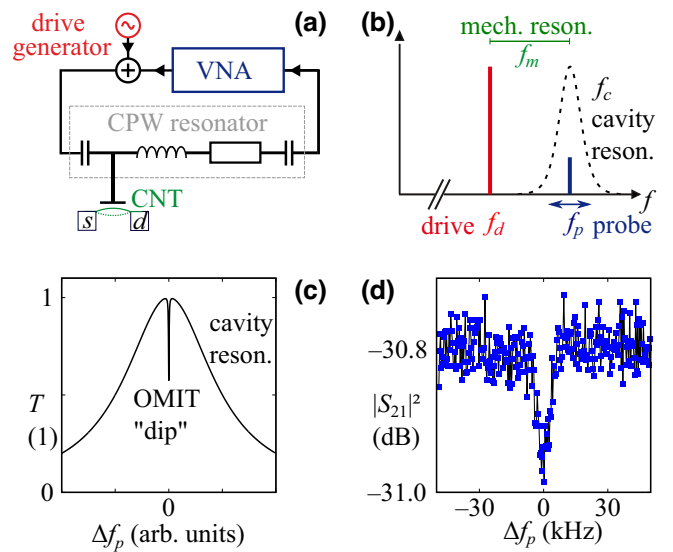

FIG. 10. (a) Circuit schematic of our optomechanically induced transparency (OMIT) experiment (simplified from [25]). (b) Signal frequency schematic. (c) Schematic plot of the cavity transmission $T = |S_{21}|^2$ [using Eq. (12)] as a function of $\Delta f_p = f_p - f_c$ for an OMIT experiment as in (a), with $f_d = f_c - f_m$. (d) Measurement of the OMIT "dip" in transmission, for $V_g = -1.187\,51$ V [cf. (c); trace from [25], Fig. 2(f)].

allowing us to treat this quantum capacitance as a replacement parameter which again depends on the deflection. With proper choice of the gate voltage working point, optomechanical experiments become possible [25].

B. Optomechanically induced (in)transparency OMIT

Our experiment for detecting and determining the optomechanical coupling is a so-called optomechanically induced transparency (OMIT) measurement, introduced first by Weis *et al.* [27] and based on earlier work on electromagnetically induced transparency of resonator media [71]. Figure 10(a) displays the simplified high-frequency circuit, while Fig. 10(b) schematically sketches the involved frequencies. A strong drive signal f_d is applied at a constant frequency red-detuned from the cavity resonance by the mechanical resonance frequency, $f_d = f_c - f_m$. Additionally a probe signal f_p is swept across the cavity resonance and its transmission measured.

Extending Eq. (1), the transmission of the probe signal, proportional to the intracavity photon number, now follows the broad peak of the electromagnetic resonance everywhere except near $f_p = f_d + f_m$, where a dip in transmission emerges [see also Fig. 10(c)]:

$$S_{21}(f_p) = \frac{2A}{4\pi i(f_c - f_p) + \Gamma_c + \frac{4g^2}{4\pi i(f_m + f_d - f_p) + \Gamma_m}} + re^{i\theta}.$$

(12)

Here, $g = \sqrt{n_c}\, g_0$ is the optomechanical coupling for the total number of cavity photons n_c, which is at fixed drive frequency proportional to the drive power. Microscopically Eq. (12) can be motivated such that mechanical phonons of frequency f_m pair up with photons of f_d, up-converting to the cavity frequency f_c, and then interfere destructively with the probe signal at f_p [27], suppressing the population of the cavity.

The width of the optomechanically induced transmission dip in Eq. (12) is given by the effective mechanical damping rate Γ_{eff} [1],

$$\Gamma_{\text{eff}} = \Gamma_m + \Gamma_{\text{opt}}, \tag{13}$$

where the latter term in the sum (see also Table III),

$$\Gamma_{\text{opt}} = \frac{4g^2}{\Gamma_c}, \tag{14}$$

is exactly the dispersive optomechanical damping (or cooling) rate induced by the red-sideband-detuned drive signal in the absence of the weak probe signal.

TABLE III. Overview of the setup and optomechanical device parameters, corresponding to the measurements of Figs. 10–12. Except for the cavity parameters evaluated separately, the values originate from the OMIT transmission curve fits and correspond to the data points in Figs. 11 and 12 for $V_g = -1.187\,54$ V.

Input signals			
Drive generator power	P_d		25 dBm
Probe (VNA) power	P_p		−20 dBm
Estimated cable damping	$|S_c|^2$		8 dB
Subsystems			
Cavity resonance frequency	f_c		5.740 05 GHz
Cavity line width	Γ_c		$2\pi \times 11.55$ MHz
Cavity quality factor	Q_c		497
Mech. resonance frequency	f_m		502.536 MHz
Mech. line width	Γ_m		$2\pi \times 5.884$ kHz
Mech. quality factor	Q_m		85 407
Coupling parameters ($n_c = 67\,500$)			
Sideband resolution	$2\pi f_m/\Gamma_c$		43.5
Single-photon coupling		g_0	$2\pi \times 94.2$ Hz
Optomechanical coupling	$g_0\sqrt{n_c}$	g	$2\pi \times 24.47$ kHz
Cavity pull-in parameter	g_0/x_{zpf}	G	$2\pi \times 50.5$ Hz/pm
Dispersive coupling	g_0/Γ_c	$\tilde{A}$	8.16×10^{-6}
Max. sideband cooling rate	$4n_c g_0^2/\Gamma_c$	Γ_{opt}	$2\pi \times 207.4$ Hz
Cooperativity	$\Gamma_{\text{opt}}/\Gamma_m$	C	0.035
Cooling power	$\Gamma_{\text{opt}} h f_m$	$\dot{Q}$	4.34×10^{-22} W

C. Quantum capacitance amplified coupling

As visible from Eq. (12), the multiphoton optomechanical coupling $g(V_g)$ as well as several other parameters can be extracted directly from OMIT measurements as curve fit parameters. This becomes particularly interesting when stepping the dc gate voltage V_g across a Coulomb oscillation and plotting the parameters as a function of gate voltage. Already well-known behavior can be seen in Fig. 11(a), with the gate voltage dependence of the mechanical resonance frequency $f_m(V_g)$, now extracted from fits of Eq. (12) to OMIT data. The decrease of $f_m(V_g)$ corresponds to the local electrostatic softening (or the "Coulomb oscillations of mechanical resonance frequency"), as also already demonstrated in Fig. 4(d) and in earlier publications [12,14,16].

Using the cavity photon number n_c as determined previously (see Fig. 9), the single-photon optomechanical coupling $g_0(V_g) = g(V_g)/\sqrt{n_c}$ can be calculated; it is plotted in Fig. 11(b) (blue points, left axis). The data clearly show maxima on the flanks of the Coulomb oscillation, while the coupling vanishes both at its center and in Coulomb blockade. This behavior has already been discussed in detail in [25]. There it was shown that $g_0(V_g)$ is connected to the time-averaged number of electrons on the quantum dot $\langle N \rangle(V_g)$, increasing by one over a Coulomb oscillation, via

$$g_0(V_g) = \left| \frac{\pi e \alpha f_c V_g}{C_{\text{RLC}} C_g} \frac{\partial C_g}{\partial x} \frac{\partial^2 \langle N \rangle}{\partial V_g^2} \right| x_{\text{zpf}}. \tag{15}$$

Assuming a lifetime-broadened level in the quantum dot and thus a Lorentzian shape of $\partial \langle N \rangle/\partial V_g$, Eq. (15) allows one to approximate the functional dependence of the $g_0(V_g)$ data in Fig. 11(b) (points) very well. In quantitative terms, theory and experiment differ by approximately
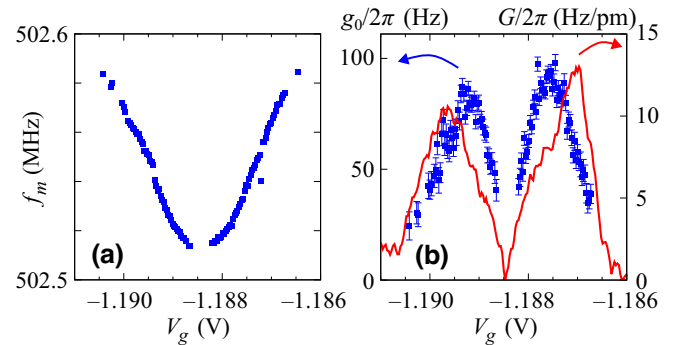

FIG. 11. OMIT-derived parameters across a Coulomb blockade oscillation, as a function of gate voltage V_g: (a) mechanical resonance frequency f_m; (b) blue points, optomechanical single photon coupling $g_0(V_g)$ [left axis, data already shown in [25], Fig. 2(g)]; red line, cavity pull-in parameter $G(V_g)$ derived from the quantum capacitance $C_q(V_g)$ of Fig. 6(b) for comparison (right axis).

a factor of 5, still an excellent agreement given the amount of approximations that enter the calculation [25].

An alternative way to characterize the optomechanical coupling is directly via the cavity pull-in parameter $G(V_g)$, that is, the cavity resonance frequency f_c shift per mechanical displacement,

$$G = \frac{g_0}{x_{zpf}} = 2\pi \frac{\partial f_c}{\partial x}. \tag{16}$$

We can extract this parameter from the gate voltage dependence of the resonance frequency $f_c(V_g)$ [Fig. 6(a)], which directly provides us the quantum capacitance $C_q(V_g)$ [Fig. 6(b)]. The details are given in Appendix B and lead to

$$G = \frac{\omega_c}{2C_{RLC}} \frac{\partial C_q}{\partial V_g} \frac{V_g}{C_g} \frac{\partial C_g}{\partial x} \tag{17}$$

where again C_g is the geometric capacitance between resonator (gate) and nanotube (quantum dot), which can be extracted rather precisely from Coulomb blockade measurements, and C_q is the quantum capacitance as plotted in Fig. 6(b).

The result for $G(V_g)$ is plotted in Fig. 11(b) as a solid red line. An offset in gate voltage has been corrected here; it was most likely caused by charging effects over the course of the lengthy measurement cooldown. The functional dependence agrees well with the OMIT result. The Coulomb oscillation structure appears to be slightly wider in gate voltage for $G(V_g)$. However, comparing the applied powers of the resonant probe signal in the OMIT case, $P_p = -20$ dBm, and the repeated cavity resonance sweeps of Fig. 6, $P = +10$ dBm, this effect is well within the possible broadening of the Coulomb oscillation by the gigahertz signal.

Since the two parameters g_0 and G are proportional and their proportionality factor $Gx_{zpf} = g_0$ is exactly the zero-point fluctuation scale of the mechanical system, this provides us a way to estimate x_{zpf}. Bringing the two curves in Fig. 11(b) to best agreement leads to $x_{zpf} = 7.4$ pm. Using the harmonic oscillator expression $x_{zpf} = \sqrt{\hbar/2m\omega_m}$ with the effective mass as given in Table II and used otherwise in the calculations, we obtain $x_{zpf} = 1.9$ pm; again the values agree to better than one order of magnitude.

Regarding error sources, for the cavity pull-in parameter $G(V_g)$ [Eq. (17)], all values can be directly read out from the measurement, with the exception of $\partial C_g/\partial x$. The latter is calculated by scaling the wire-over-plane model for a gated CNT [25,48] down to the effective electronic length $\ell_{eff} = 140$ nm of the nanotube quantum dot: we calculate the theoretical capacitance between suspended nanotube and gate from the device geometry, compare it with the Coulomb blockade derived gate capacitance C_g to obtain an effective electronic length, and scale the theoretical derivative $\partial C_g/\partial x$ accordingly.

Conversely, the main error source for the single- photon optomechanical coupling $g_0(V_g)$ from [25] is the cavity photon number n_c, derived with the assumption that the gate electrode shows the same gigahertz voltage amplitude as the end of the CPW resonator at its coupling capacitance (and voltage antinode). This error could be reduced by, for example, more detailed finite-element modeling of the device. However, since the exact position and orientation of the deposited CNT are unknown in the experiment, it is unclear whether the additional effort would be of much help.

D. Damping of the motion in OMIT

Figure 12(a) plots the mechanical quality factor Q_m extracted from OMIT via Eq. (12). Q_m displays two distinct minima on the Coulomb oscillation flanks, and on the whole a behavior inverse to the optomechanical coupling $g = \sqrt{n_c}g_0$. This is clearly different from damping induced by electronic tunneling alone [see, for example, Meerwaldt *et al.* [68]], where for $V_{sd} \simeq 0$ only a single minimum of the quality factor is observed.
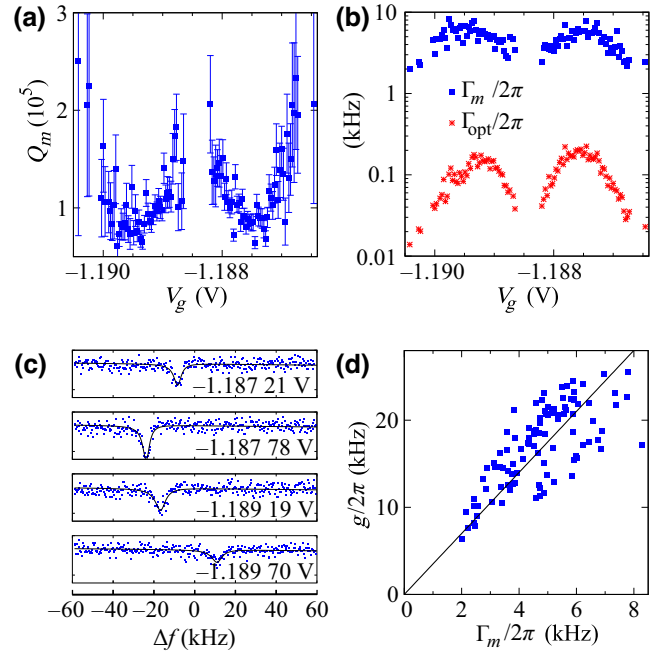

FIG. 12. (a) Mechanical quality factor $Q_m = 2\pi f_m/\Gamma_m$ observed during the OMIT experiment, as a function of gate voltage V_g. (b) Mechanical damping rate Γ_m (blue squares) and optomechanical damping rate $\Gamma_{opt} = 4g^2/\Gamma_c$ (red stars) from the OMIT measurement. Both g and Γ_m have been obtained via fitting Eq. 12. (c) Example raw data traces of the OMIT measurement, showing the OMIT "dip" in transmission $|S_{21}(f)|^2$ at different gate voltages. (d) Optomechanical coupling g plotted as a function of the corresponding observed damping Γ_m. The solid line is a linear fit $g = a\Gamma_m$ to all data points, resulting in $a = 3.5$.

The total, effective damping rate of the mechanical system taking into account optomechanical coupling is given by Eq. (13), combining mechanical behavior and the damping via up-conversion of the red-detuned drive signal. For comparison of scales, the extracted damping rate Γ_m, inversely proportional to Q_m, varies in the range $2\,\text{kHz} \le \Gamma_m/(2\pi) \le 9\,\text{kHz}$. At the same time, we find $8\,\text{Hz} \le \Gamma_{\text{opt}}/(2\pi) \le 215\,\text{Hz}$. This indicates that even at our enhanced optomechanical coupling the damping via up-conversion from Eq. (13) is small in the experiment. Figure 12(b) plots both values as a function of V_g, confirming this conclusion with a nearly two orders of magnitude smaller optomechanical damping for any gate voltage.

An apparent variation in Q_m and the width of the OMIT dip can be caused by mechanically nonlinear behavior. Equation (12) assumes a harmonic oscillator; if strong driving leads to a distortion of the mechanical resonance shape toward a Duffing curve, the fit will return artificially smaller Q_m values. Figure 12(c) plots several raw data curves of the frequency-dependent power transmission as examples. While occasionally asymmetric curve shapes can be observed in the raw data with its scatter, no systematic gate voltage dependence of this nonlinear behavior emerges. Thus, no conclusion about the impact of nonlinearity on the fit results can be drawn.

In Fig. 12(d), the data behind Fig. 12(a) are plotted showing $g(\Gamma_m)$, that is, the optomechanical coupling g as a function of the mechanical damping Γ_m (extracted from the fits); the plot indicates a possible linear relation between the two parameters. The cause of this linear relation is so far unknown; it may be due to a more complex interaction of Coulomb blockade, mechanics, and the microwave fields. A large body of theoretical literature and also experiments on the interaction of coherent superconducting qubit systems and optomechanical systems exists; see also below. However, the detailed properties differ from our single-electron tunneling case, such that, for example, results from [72] on the damping cannot be directly transferred.

V. CONCLUSIONS AND OUTLOOK

A piece-by-piece characterization of an optomechanical device has been presented, combining a suspended CNT as quantum dot and mechanical resonator with a superconducting coplanar microwave resonator [25]. The properties of the three separate subsystems have been discussed in detail, as have their pairwise interactions. This includes the dispersion of the observed mechanical modes and their interaction with single-electron tunneling, as well as the direct impact of the nanotube quantum dot on the coplanar resonator transmission phase and damping. Subsequently, the combined device has been introduced as a quantum capacitance enhanced optomechanical system. Its

properties, as already shown in [25], are presented and the discussion is significantly extended.

An alternative evaluation based on measuring the full cavity transmission curve allows us to estimate the zero-point motion scale x_{zpf} of the nanotube, with the result well within expected range. Further, the gate voltage dependence of the damping of the mechanical system during an OMIT experiment is extracted. We find that the observed functional dependence cannot be explained by Coulomb blockade, nanoelectromechanical interaction, or optomechanics alone, indicating a more complex mechanism. Different evaluation paths of the measurements on device and subsystems lead to near-equivalent results, indicating a high degree of consistency of our total data set.

Starting from the initial experiment combining transmon qubit and a cavity with a nanomechanical resonator [73], much theoretical [74–79] and experimental work [72,80] has been invested worldwide in similar superconducting systems. This includes generic qubit treatment, but also specifically the importance of the Josephson inductance [75,76] and the Josephson capacitance [81]. Damping mechanisms are experimentally analyzed in [72]. However, given the sequential electronic tunneling in our normal-conducting CNT quantum dot, it is not *a priori* clear how far these discussions apply to our work. They are certainly closer to the situation of a double quantum dot as charge qubit [see also [82], for example], and would certainly be relevant for a CNT as weak link modulating an optomechanical system via Josephson inductance [75,76,83].

Given that the nanotube motion affects both the cavity resonance frequency and the cavity linewidth (see Fig. 6), a remaining open question is whether additional dissipative optomechanical coupling [84–87] plays a role here. From a theoretical viewpoint, the central advantage of dissipative optomechanical coupling is that it does not require the "good cavity limit" $2\pi f_m \gg \Gamma_c$ for eventual ground-state cooling of the mechanical system [84]; in the present experiment with $2\pi f_m/\Gamma_c \simeq 44$, however, this limitation of dispersive coupling is not relevant. In addition, the prototypical dissipative system of [84,85] assumes an overdamped cavity where coupling to the drive port limits Q_c, an assumption far from the device parameters of our strongly underdamped resonator with maximum transmission below -50 dB. This is a topic which can be addressed in future better-suited devices.

Regarding further future research, the obvious path is to improve the coupling and subsystem parameters; given the already surprising results of Table III (updated with respect to [25] to reflect the more precise evaluation of the mechanical resonance), reaching strong optomechanical coupling is likely within realistic technological reach. Sharper Coulomb oscillations via a lower electronic tunnel rate Γ (and possibly lower electronic temperature and better filtering of voltage fluctuations) can compress the

charge increase into a smaller potential range. This will increase the quantum capacitance-mediated coupling g_0, as long as the separation of time scales via $\Gamma \gg 2\pi f_c$ holds. Ongoing work targets the circuit geometry [88], adding on-chip filters to avoid gigahertz leakage through the dc contacts and thus achieving larger resonator quality factors Q_c. Further options which may be considered in the future include an entirely changed circuit layout and the use of high kinetic inductance materials to maximize the impact of a changing capacitance at constant resonance frequency f_c.

Physically, the time-dependent evolution of the coupled system is certainly a worthwhile object of investigation, as are coherence effects comparing single- and multi-quantum dot systems, and implications of more complex optomechanical coupling mechanisms [79,89,90].

AUTHOR CONTRIBUTIONS

A.K.H. and S.B. conceived and designed the experiment. P.S. and R.G. developed and performed nanotube growth and transfer; N.H. and S.B. developed and fabricated the CPW device. The low-temperature measurements were performed jointly by all authors. Data evaluation was done jointly by S.B., N.H., and A.K.H. The manuscript was written by N.H. and A.K.H. with help from A.N.L.; the project was supervised by A.K.H.

APPENDIX A: PHOTON NUMBER

The estimation of the resonator photon number in Sec. III C has two limitations. On the one hand, it assumes that the ac gate voltage acting on the quantum dot is equal to the ac voltage at the voltage antinode (i.e., the coupling capacitor) of the microwave resonator. In reality, the ac gate voltage is likely smaller: the gate finger is attached close to but not at the end of the resonator, and along its length the voltage amplitude can vary as well. Note that the gate electrode is a 100-nm-wide gold strip, and accordingly has finite ohmic resistance as well as a geometry not

adapted to $Z_0 = 50\ \Omega$. This leads to an underestimation of n_c.

On the other hand, the CPW resonator is strongly undercoupled. This leads to an asymmetry of signal level between input (drive) and output (detection) port, for both the resonant case and for the off-resonant case. Figure 13 illustrates this with a numerical calculation of our bare resonator geometry (i.e., only the niobium layer and no further fabrication) using Sonnet Professional [92–94]. Modeling the full chip is significantly more difficult because of the large differences in scale between meander filters and electrodes on one hand and the full CPW resonator on the other hand [88]. The signal transmission $|S_{21}|^2$, plotted as a function of frequency in Fig. 13(a), reaches in the calculation a maximum of -67 dB at resonance $f \simeq 5.27$ GHz.

The current distribution of the Sonnet calculation is plotted in Fig. 13(b) for $f = 4.4$ GHz, that is, a strongly detuned red sideband drive as in our measurement. A closer look shows that in particular for such an off-resonant drive signal, direct crosstalk between the input port and the nearby nanotube contact electrodes (indicated by a black
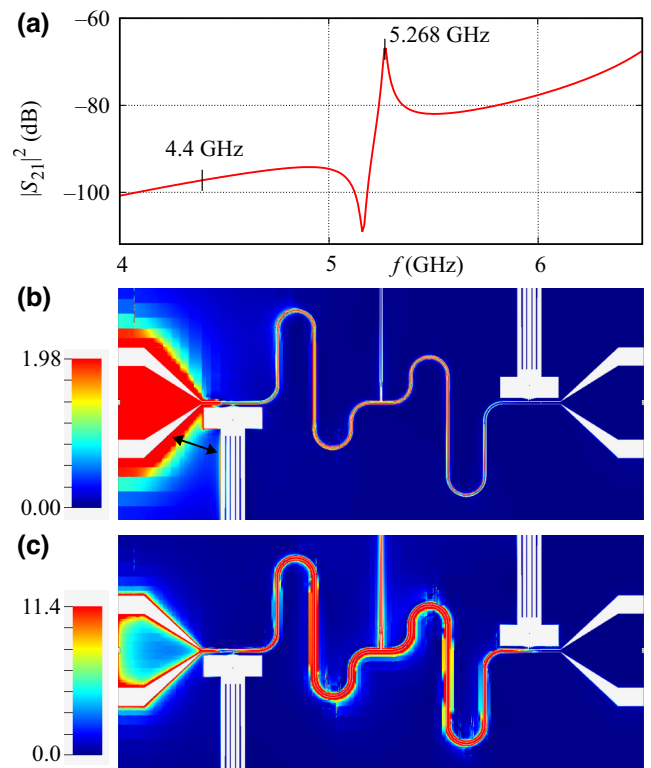

FIG. 13. Numerical calculation using Sonnet [92] of the gigahertz response of the bare niobium resonator chip geometry (i.e., only patterned niobium on the substrate, no further metallizations or structuring). (a) Transmission $|S_{21}|^2$ as a function of frequency. The frequencies of (b),(c) are marked in the plot. (b),(c) Detail zoom of the rf current distribution for a drive at (b) $f = 4.4$ GHz (off-resonant) and (c) $f = 5.268$ GHz (resonant in the calculation) (arbitrary units).

arrow) can cause additional ac signals on the nanotube. In the evaluation of Sec. III C this can lead to an overestimation of n_c. Future device design will have to take this error mechanism into account.

An alternative estimate for the resonator photon number can be performed using the nominal attenuation and amplification values of the microwave setup. Following [95], we calculate the photon number in the resonant case $f = f_c = 5.74$ GHz, $Q = 497$, for a VNA output power of 25 dBm. With the attenuation in the input cable of -53 dB excluding the cable loss, and a cable loss in both input and output each of -8 dB, the resulting incoming power at the resonator input port is -36 dBm; see also the circuit scheme of Fig. 2(a).

At resonance, we measure on the VNA a transmission attenuation of -49.6 dB; considering the 90 dB amplification of low temperature and room temperature amplifiers and again the cable loss, we obtain -106.6 dBm as the power leaving the resonator.

This results in an insertion loss of

$$\text{IL} = \frac{P_{\text{out}}}{P_{\text{in}}} = -70.6 \text{ dB}, \tag{A1}$$

allowing us to calculate the circulating power

$$P_{\text{circ}} = P_{\text{in}} Q \times 10^{\text{IL}/20}/\pi = 11.7 \text{ nW}, \tag{A2}$$

and finally the photon number in the resonator for the resonant driving case,

$$n_{\text{res}} = \frac{P_{\text{circ}}}{hf_c^2} = 537\,000. \tag{A3}$$

To obtain the photon number for the red sideband drive case we multiply n_{res} by the ratio $|S_{21}(f)/S_{21}(f_c)|^2$, resulting in $n(25 \text{ dBm}) = 72$, or at the drive power of the OMIT experiments $n(20 \text{ dBm}) = 23$, respectively.

The value of $n_c = 21\,300$ derived from the calibration in the main text is much larger. However, it is consistent with the broadening of the Coulomb oscillation in Fig. 9(a). Additionally, a much smaller photon number would result in an even much larger single-photon coupling via the OMIT experiment than already found, at the risk of an equally large overestimation of our already large Coulomb-blockade enhancement of the optomechanical coupling. While this naturally gives rise to optimism, it will have to be confirmed in future experiments.

APPENDIX B: CAVITY PULL PARAMETER

The frequency shift per displacement or cavity pull parameter G is defined as

$$G = \frac{\partial \omega_c}{\partial x}\bigg|_{x=0}. \tag{B1}$$

In a microwave optomechanical system with a deflection-dependent cavity (replacement) capacitance C_{RLC}, using the relation $\omega_c = 1/\sqrt{C_{\text{RLC}} L_{\text{RLC}}}$, it can be written as

$$G = \frac{\omega_c}{2C_{\text{RLC}}} \frac{\partial C_{\text{RLC}}}{\partial x}\bigg|_{x=0}. \tag{B2}$$

Applying the same logic as in [25], Supplement, Eqs. (26)–(29), we can translate a capacitance modulation into an effective gate voltage modulation via $C_g \, \partial V_g = V_g \, \partial C_g$ and write G as

$$G = \frac{\omega_c}{2C_{\text{RLC}}} \frac{\partial C_{\text{RLC}}}{\partial V_g} \frac{V_g}{C_g} \frac{\partial C_g}{\partial x} \tag{B3}$$

where C_g is the geometric capacitance between resonator (gate) and nanotube (quantum dot).

[1] M. Aspelmeyer, T. J. Kippenberg, and F. Marquardt, Cavity optomechanics, Rev. Mod. Phys. **86**, 1391 (2014).

[2] Jasper Chan, T. P. Mayer Alegre, Amir H. Safavi-Naeini, Jeff T. Hill, Alex Krause, Simon Groeblacher, Markus Aspelmeyer, and Oskar Painter, Laser cooling of a nanomechanical oscillator into its quantum ground state, Nature **478**, 89 (2011).

[3] J. D. Teufel, T. Donner, Dale Li, J. W. Harlow, M. S. Allman, K. Cicak, A. J. Sirois, J. D. Whittaker, K. W. Lehnert, and R. W. Simmonds, Sideband cooling of micromechanical motion to the quantum ground state, Nature **475**, 359 (2011).

[4] F. Lecocq, J. B. Clark, R. W. Simmonds, J. Aumentado, and J. D. Teufel, Quantum nondemolition measurement of a nonclassical state of a massive object, Phys. Rev. X **5**, 041037 (2015).

[5] J. D. Teufel, T. Donner, M. A. Castellanos-Beltran, J. W. Harlow, and K. W. Lehnert, Nanomechanical motion measured with an imprecision below that at the standard quantum limit, Nat. Nanotechnol. **4**, 820 (2009).

[6] Michael Metcalfe, Applications of cavity optomechanics, Appl. Phys. Rev. **1**, 031105 (2014).

[7] A. K. Hüttel, G. A. Steele, B. Witkamp, M. Poot, L. P. Kouwenhoven, and H. S. J. van der Zant, Carbon nanotubes as ultrahigh quality factor mechanical resonators, Nano Lett. **9**, 2547 (2009).

[8] J. Moser, A. Eichler, J. Güttinger, M. I. Dykman, and A. Bachtold, Nanotube mechanical resonators with quality factors of up to 5 million, Nat. Nanotechnol. **9**, 1007 (2014).

[9] E. A. Laird, F. Kuemmeth, G. A. Steele, K. Grove-Rasmussen, J. Nygård, K. Flensberg, and L. P. Kouwenhoven, Quantum transport in carbon nanotubes, Rev. Mod. Phys. **87**, 703 (2015).

[10] M. Margańska, D. R. Schmid, A. Dirnaichner, P. L. Stiller, Ch. Strunk, M. Grifoni, and A. K. Hüttel, Shaping electron wave functions in a carbon nanotube with a parallel magnetic field, Phys. Rev. Lett. **122**, 086802 (2019).

[11] Daniel R. Schmid, Peter L. Stiller, Alois Dirnaichner, and Andreas K. Hüttel, From transparent conduction to

Coulomb blockade at fixed hole number, Phys. Status Solidi (B) **257,** 2000253 (2020).

[12] G. A. Steele, A. K. Hüttel, B. Witkamp, M. Poot, H. B. Meerwaldt, L. P. Kouwenhoven, and H. S. J. van der Zant, Strong coupling between single-electron tunneling and nanomechanical motion, Science **325,** 1103 (2009).

[13] B. Lassagne, Y. Tarakanov, J. Kinaret, D. Garcia-Sanchez, and A. Bachtold, Coupling mechanics to charge transport in carbon nanotube mechanical resonators, Science **325,** 1107 (2009).

[14] A. K. Hüttel, H. B. Meerwaldt, G. A. Steele, M. Poot, B. Witkamp, L. P. Kouwenhoven, and H. S. J. van der Zant, Single electron tunnelling through high-*Q* single-wall carbon nanotube NEMS resonators, Phys. Status Solidi (b) **247,** 2974 (2010).

[15] P. Häkkinen, A. Isacsson, A. Savin, J. Sulkko, and P. Hakonen, Charge sensitivity enhancement via mechanical oscillation in suspended carbon nanotube devices, Nano Lett. **15,** 1667 (2015).

[16] K. J. G. Götz, D. R. Schmid, F. J. Schupp, P. L. Stiller, Ch. Strunk, and A. K. Hüttel, Nanomechanical characterization of the Kondo charge dynamics in a carbon nanotube, Phys. Rev. Lett. **120,** 246802 (2018).

[17] J. J. Viennot, M. C. Dartiailh, A. Cottet, and T. Kontos, Coherent coupling of a single spin to microwave cavity photons, Science **349,** 408 (2015).

[18] M. M. Desjardins, J. J. Viennot, M. C. Dartiailh, L. E. Bruhat, M. R. Delbecq, M. Lee, M.-S. Choi, A. Cottet, and T. Kontos, Observation of the frozen charge of a Kondo resonance, Nature **545,** 71 (2017).

[19] S. Stapfner, L. Ost, D. Hunger, J. Reichel, I. Favero, and E. M. Weig, Cavity-enhanced optical detection of carbon nanotube Brownian motion, Appl. Phys. Lett. **102,** 151910 (2013).

[20] M. Zhang, A. Barnard, P. L. McEuen, and M. Lipson, in *CLEO: 2014*, OSA Technical Digest (online) (Optica Publishing Group, 2014), p. FTu2B.1.

[21] A. Tavernarakis, A. Stavrinadis, A. Nowak, I. Tsioutsios, A. Bachtold, and P. Verlot, Optomechanics with a hybrid carbon nanotube resonator, Nat. Commun. **9,** 662 (2018).

[22] A. W. Barnard, M. Zhang, G. S. Wiederhecker, M. Lipson, and P. L. McEuen, Real-time vibrations of a carbon nanotube, Nature **566,** 89 (2019).

[23] C. A. Regal, J. D. Teufel, and K. W. Lehnert, Measuring nanomechanical motion with a microwave cavity interferometer, Nat. Phys. **4,** 555 (2008).

[24] Soumya Ranjan Das, Sourav Majumder, Sudhir Kumar Sahu, Ujjawal Singhal, Tanmoy Bera, and Vibhor Singh, Instabilities near ultrastrong coupling in a microwave optomechanical cavity, Phys. Rev. Lett. **131,** 067001 (2023).

[25] S. Blien, P. Steger, N. Hüttner, R. Graaf, and A. K. Hüttel, Quantum capacitance mediated carbon nanotube optomechanics, Nat. Commun. **11,** 1363 (2020).

[26] G. S. Agarwal and Sumei Huang, Electromagnetically induced transparency in mechanical effects of light, Phys. Rev. A **81,** 041803 (2010).

[27] S. Weis, R. Rivière, S. Deléglise, E. Gavartin, O. Arcizet, A. Schliesser, and T. J. Kippenberg, Optomechanically induced transparency, Science **330,** 1520 (2010).

[28] L. P. Kouwenhoven, C. M. Marcus, P. L. McEuen, S. Tarucha, R. M. Westervelt, and N. S. Wingreen, in *Mesoscopic Electron Transport*, edited by L. L. Sohn, L. P. Kouwenhoven, and G. Schön (Kluwer, Dordrecht, 1997).

[29] David M. Pozar, *Microwave Engineering* (John Wiley & Sons, Inc., Hoboken, NJ, 2012), 4th ed.

[30] R. N. Simons, *Coplanar Waveguide Circuits, Components, and Systems* (John Wiley & Sons, Inc., Hoboken, NJ, 2001).

[31] S. Gevorgian, L. J. P. Linner, and E. L. Kollberg, CAD models for shielded multilayered CPW, IEEE Trans. Microw. Theory Tech. **43,** 772 (1995).

[32] K. D. Petersson, L. W. McFaul, M. D. Schroer, M. Jung, J. M. Taylor, A. A. Houck, and J. R. Petta, Circuit quantum electrodynamics with a spin qubit, Nature **490,** 380 (2012).

[33] M. Göppl, A. Fragner, M. Baur, R. Bianchetti, S. Filipp, J. M. Fink, P. J. Leek, G. Puebla, L. Steffen, and A. Wallraff, Coplanar waveguide resonators for circuit quantum electrodynamics, J. Appl. Phys. **104,** 113904 (2008).

[34] J. M. Hornibrook, E. E. Mitchell, and D. J. Reilly, Superconducting resonators with parasitic electromagnetic environments, ArXiv:1203.4442 (2012).

[35] M. S. Khalil, M. J. A. Stoutimore, F. C. Wellstood, and K. D. Osborn, An analysis method for asymmetric resonator transmission applied to superconducting devices, J. Appl. Phys. **111,** 054510 (2012).

[36] P. J. Petersan and S. M. Anlage, Measurement of resonant frequency and quality factor of microwave resonators: Comparison of methods, J. Appl. Phys. **84,** 3392 (1998).

[37] V. Singh, S. J. Bosman, B. H. Schneider, Y. M. Blanter, A. Castellanos-Gomez, and G. A. Steele, Optomechanical coupling between a multilayer graphene mechanical resonator and a superconducting microwave cavity, Nat. Nanotechnol. **9,** 820 (2014).

[38] S. Blien, K. J. G. Götz, P. L. Stiller, T. Mayer, T. Huber, O. Vavra, and A. K. Hüttel, Towards carbon nanotube growth into superconducting microwave resonator geometries, Phys. Status Solidi (b) **253,** 2385 (2016).

[39] Yu Hao, Francisco Rouxinol, and M. D. LaHaye, Development of a broadband reflective T-filter for voltage biasing high-Q superconducting microwave cavities, Appl. Phys. Lett. **105,** 222603 (2014).

[40] C. C. Wu, C. H. Liu, and Z. Zhong, One-step direct transfer of pristine single-walled carbon nanotubes for functional nanoelectronics, Nano Lett. **10,** 1032 (2010).

[41] S. Blien, P. Steger, A. Albang, N. Paradiso, and A. K. Hüttel, Quartz tuning-fork based carbon nanotube transfer into quantum device geometries, Phys. Status Solidi (b) **255,** 1800118 (2018).

[42] Sander J. Tans, Michel H. Devoret, Hongjie Dai, Andreas Thess, Richard E. Smalley, L. J. Geerligs, and Cees Dekker, Individual single-wall carbon nanotubes as quantum wires, Nature **386,** 474 (1997).

[43] S. Braig and K. Flensberg, Vibrational sidebands and dissipative tunneling in molecular transistors, Phys. Rev. B **68,** 205324 (2003).

[44] J. Koch and F. von Oppen, Franck-Condon blockade and giant Fano factors in transport through single molecules, Phys. Rev. Lett. **94,** 206804 (2005).

[45] S. Sapmaz, P. Jarillo-Herrero, Ya. M. Blanter, C. Dekker, and H. S. J. van der Zant, Tunneling in suspended carbon

nanotubes assisted by longitudinal phonons, Phys. Rev. Lett. **96**, 026801 (2006).

[46] A. K. Hüttel, B. Witkamp, M. Leijnse, M. R. Wegewijs, and H. S. J. van der Zant, Pumping of vibrational excitations in the Coulomb-blockade regime in a suspended carbon nanotube, Phys. Rev. Lett. **102**, 225501 (2009).

[47] P. L. Stiller, A. Dirnaichner, D. R. Schmid, and A. K. Hüttel, Magnetic field control of the Franck-Condon coupling of few-electron quantum states, Phys. Rev. B **102**, 115408 (2020).

[48] O. Wunnicke, Gate capacitance of back-gated nanowire field-effect transistors, Appl. Phys. Lett. **89**, 083102 (2006).

[49] D. R. Schmid, P. L. Stiller, C. Strunk, and A. K. Hüttel, Magnetic damping of a carbon nanotube nano-electromechanical resonator, New J. Phys. **14**, 083024 (2012).

[50] D. R. Schmid, P. L. Stiller, Ch. Strunk, and A. K. Hüttel, Liquid-induced damping of mechanical feedback effects in single electron tunneling through a suspended carbon nanotube, Appl. Phys. Lett. **107**, 123110 (2015).

[51] Sharon Rechnitz, Tal Tabachnik, Michael Shlafman, Shlomo Shlafman, and Yuval E. Yaish, Mode coupling bi-stability and spectral broadening in buckled carbon nanotube mechanical resonators, Nat. Commun. **13**, 5900 (2022).

[52] V. Sazonova, Y. Yaish, H. Üstünel, D. Roundy, T. A. Arias, and P. L. McEuen, A tunable carbon nanotube electromechanical oscillator, Nature **431**, 284 (2004).

[53] B. Witkamp, M. Poot, and H. S. J. van der Zant, Bending-mode vibration of a suspended nanotube resonator, Nano Lett. **6**, 2904 (2006).

[54] Karl J. G. Götz, Felix J. Schupp, and Andreas K. Hüttel, Carbon nanotube millikelvin transport and nanomechanics, Phys. Status Solidi (b) **256**, 1800517 (2019).

[55] Vincent Gouttenoire, Thomas Barois, Sorin Perisanu, Jean-Louis Leclercq, Stephen T. Purcell, Pascal Vincent, and Anthony Ayari, Digital and FM demodulation of a doubly clamped single-walled carbon-nanotube oscillator: Towards a nanotube cell phone, Small **6**, 1060 (2010).

[56] Young-Kyun Kwon, Savas Berber, and David Tománek, Thermal contraction of carbon fullerenes and nanotubes, Phys. Rev. Lett. **92**, 015901 (2004).

[57] Nicolas Mounet and Nicola Marzari, First-principles determination of the structural, vibrational and thermodynamic properties of diamond, graphite, and derivatives, Phys. Rev. B **71**, 205214 (2005).

[58] Alexander A. Balandin, Thermal properties of graphene and nanostructured carbon materials, Nat. Mater. **10**, 569 (2011).

[59] Xiannian Chi, Lei Wang, Jian Zhang, Jean Pierre Nshimiyimana, Xiao Hu, Pei Wu, Siyu Liu, Jia Liu, Weiguo Chu, Qian Liu, and Lianfeng Sun, Experimental evidence of negative thermal expansion in a composite nanocable of single-walled carbon nanotubes and amorphous carbon along the axial direction, J. Phys. Chem. C **122**, 26707 (2018).

[60] I. Kozinsky, H. W. Ch. Postma, I. Bargatin, and M. L. Roukes, Tuning nonlinearity, dynamic range, and frequency of nanomechanical resonators, Appl. Phys. Lett. **88**, 253101 (2006).

[61] C. C. Wu and Z. Zhong, Capacitive spring softening in single-walled carbon nanotube nanoelectromechanical resonators, Nano Lett. **11**, 1448 (2011).

[62] P. L. Stiller, S. Kugler, D. R. Schmid, C. Strunk, and A. K. Hüttel, Negative frequency tuning of a carbon nanotube nano-electromechanical resonator under tension, Phys. Status Solidi (b) **250**, 2518 (2013).

[63] A. Eichler, M. del Álamo Ruiz, J. A. Plaza, and A. Bachtold, Strong coupling between mechanical modes in a nanotube resonator, Phys. Rev. Lett. **109**, 025503 (2012).

[64] A. Eichler, J. Moser, J. Chaste, M. Zdrojek, I. Wilson-Rae, and Adrian Bachtold, Nonlinear damping in mechanical resonators made from carbon nanotubes and graphene, Nat. Nanotechnol. **6**, 339 (2011).

[65] Hari S. Solanki, Shamashis Sengupta, Sajal Dhara, Vibhor Singh, Sunil Patil, Rohan Dhall, Jeevak Parpia, Arnab Bhattacharya, and Mandar M. Deshmukh, Tuning mechanical modes and influence of charge screening in nanowire resonators, Phys. Rev. B **81**, 115459 (2010).

[66] M. R. Delbecq, V. Schmitt, F. D. Parmentier, N. Roch, J. J. Viennot, G. Fève, B. Huard, C. Mora, A. Cottet, and T. Kontos, Coupling a quantum dot, fermionic leads, and a microwave cavity on a chip, Phys. Rev. Lett. **107**, 256804 (2011).

[67] Leif Roschier, Mika Sillanpää, and Pertti Hakonen, Quantum capacitive phase detector, Phys. Rev. B **71**, 024530 (2005).

[68] H. B. Meerwaldt, G. Labadze, B. H. Schneider, A. Taspinar, Ya. M. Blanter, H. S. J. van der Zant, and G. A. Steele, Probing the charge of a quantum dot with a nanomechanical resonator, Phys. Rev. B **86**, 115454 (2012).

[69] R. Schleser, E. Ruh, T. Ihn, K. Ensslin, D. C. Driscoll, and A. C. Gossard, Finite-bias charge detection in a quantum dot, Phys. Rev. B **72**, 035312 (2005).

[70] C. W. J. Beenakker, Theory of Coulomb-blockade oscillations in the conductance of a quantum dot, Phys. Rev. B **44**, 1646 (1991).

[71] K.-J. Boller, A. Imamoğlu, and S. E. Harris, Observation of electromagnetically induced transparency, Phys. Rev. Lett. **66**, 2593 (1991).

[72] J.-M. Pirkkalainen, S. U. Cho, F. Massel, J. Tuorila, T. T. Heikkilä, P. J. Hakonen, and M. A. Sillanpää, Cavity optomechanics mediated by a quantum two-level system, Nat. Commun. **6**, 6981 (2015).

[73] J.-M. Pirkkalainen, S. U. Cho, Jian Li, G. S. Paraoanu, P. J. Hakonen, and M. A. Sillanpää, Hybrid circuit cavity quantum electrodynamics with a micromechanical resonator, Nature **494**, 211 (2013).

[74] Anika C. Pflanzer, Oriol Romero-Isart, and J. Ignacio Cirac, Optomechanics assisted by a qubit: From dissipative state preparation to many-partite systems, Phys. Rev. A **88**, 033804 (2013).

[75] T. T. Heikkilä, F. Massel, J. Tuorila, R. Khan, and M. A. Sillanpää, Enhancing optomechanical coupling via the Josephson effect, Phys. Rev. Lett. **112**, 203603 (2014).

[76] A. J. Rimberg, M. P. Blencowe, A. D. Armour, and P. D. Nation, A cavity-Cooper pair transistor scheme for investigating quantum optomechanics in the ultra-strong coupling regime, New J. Phys. **16**, 055008 (2014).

[77] Mehdi Abdi, Matthias Pernpeintner, Rudolf Gross, Hans Huebl, and Michael J. Hartmann, Quantum state engineering with circuit electromechanical three-body interactions, Phys. Rev. Lett. **114**, 173602 (2015).

[78] Vera Gramich, Björn Kubala, Selina Rohrer, and Joachim Ankerhold, From Coulomb-blockade to nonlinear quantum dynamics in a superconducting circuit with a resonator, Phys. Rev. Lett. **111**, 247002 (2013).

[79] Raphaël Khan, F. Massel, and T. T. Heikkilä, Cross-Kerr nonlinearity in optomechanical systems, Phys. Rev. A **91**, 043822 (2015).

[80] Philip Schmidt, Mohammad T. Amawi, Stefan Pogorzalek, Frank Deppe, Achim Marx, Rudolf Gross, and Hans Huebl, Sideband-resolved resonator electromechanics based on a nonlinear Josephson inductance probed on the single-photon level, Commun. Phys. **3**, 1 (2020).

[81] Juuso Manninen, Mohammad Tasnimul Haque, David Vitali, and Pertti Hakonen, Enhancement of the optomechanical coupling and Kerr nonlinearity using the Josephson capacitance of a Cooper-pair box, Phys. Rev. B **105**, 144508 (2022).

[82] F. Pistolesi, A. N. Cleland, and A. Bachtold, Proposal for a nanomechanical qubit, Phys. Rev. X **11**, 031027 (2021).

[83] Jukka-Pekka Kaikkonen, Abhilash Thanniyil Sebastian, Patrik Laiho, Nan Wei, Marco Will, Yongping Liao, Esko I. Kauppinen, and Pertti J. Hakonen, Suspended superconducting weak links from aerosol-synthesized single-walled carbon nanotubes, Nano Res. **13**, 3433 (2020).

[84] Florian Elste, S. M. Girvin, and A. A. Clerk, Quantum noise interference and backaction cooling in cavity nanomechanics, Phys. Rev. Lett. **102**, 207209 (2009).

[85] Florian Elste, A. A. Clerk, and S. M. Girvin, Erratum: Quantum noise interference and backaction cooling in cavity nanomechanics [Phys. Rev. Lett. 102, 207209 (2009)], Phys. Rev. Lett. **103**, 149902 (2009).

[86] Mo Li, Wolfram H. P. Pernice, and Hong X. Tang, Reactive cavity optical force on microdisk-coupled nanomechanical beam waveguides, Phys. Rev. Lett. **103**, 223901 (2009).

[87] Talitha Weiss, Christoph Bruder, and Andreas Nunnenkamp, Strong-coupling effects in dissipatively coupled optomechanical systems, New J. Phys. **15**, 045017 (2013).

[88] N. Kellner, N. Hüttner, M. Will, P. Hakonen, and A. K. Hüttel, Stepwise fabrication and optimization of coplanar waveguide resonator hybrid devices, Phys. Status Solidi (b), 2300187 (2023).

[89] Wei Xiong, Da-Yu Jin, Yueyin Qiu, Chi-Hang Lam, and J. Q. You, Cross-Kerr effect on an optomechanical system, Phys. Rev. A **93**, 023844 (2016).

[90] Dan Hu, Shang-Yu Huang, Jie-Qiao Liao, Lin Tian, and Hsi-Sheng Goan, Quantum coherence in ultrastrong optomechanics, Phys. Rev. A **91**, 013812 (2015).

[91] S. Reinhardt, C. Butschkow, S. Geissler, A. Dirnaichner, F. Olbrich, C. Lane, D. Schröer, and A. K. Hüttel, Lab::Measurement—A portable and extensible framework for controlling lab equipment and conducting measurements, Comput. Phys. Commun. **234**, 216 (2019).

[92] Sonnet Software, Inc., https://www.sonnetsoftware.com/products/sonnet-suites/ Sonnet Professional 18.56 (2022), a detailed list of references for the used algorithms can be found on the product website.

[93] J. C. Rautio and R. F. Harrington, An electromagnetic time-harmonic analysis of shielded microstrip circuits, IEEE Trans. Microw. Theory Tech. **35**, 726 (1987).

[94] Roger F. Harrington, *Field Computation by Moment Methods*, IEEE Press Series on Electromagnetic Waves (IEEE Press, Piscataway, NJ, 1993).

[95] Jeremy M. Sage, Vladimir Bolkhovsky, William D. Oliver, Benjamin Turek, and Paul B. Welander, Study of loss in superconducting coplanar waveguide resonators, J. Appl. Phys. **109**, 063915 (2011).